New mechanistic cutting force model for milling additive manufactured Inconel 718 considering effects of tool wear evolution and actual tool geometry.

Edouard Ducroux [1*], Guillaume Fromentin [1], Fabien Viprey [1], David Prat [1], Alain D'Acunto [2]

1 : Laboratoire Bourguignon des Matériaux et Procédés [LABOMAP], Arts et Métiers Institut de Technologie

2 : Laboratoire d'Etude des Microstructures et de Mécanique des Matériaux [LEM3], Arts et Métiers Institut de Technologie

* Corresponding author at :edouard.ducroux@ensam.eu

Abstract:

Inconel 718 is widely used in aircraft industry due to its properties. Nevertheless, its mechanical and chemical properties make it hard-to-cut. As a consequence, additive manufacturing is developed in order to get near net shape part before machining. Thus, this article presents a study on the machinability of the Inconel 718 obtained by additive manufacturing compare to one from wrought bar. Firstly, the machinability in milling is investigated through microstructure observation and cutting forces analysis, then a tool wear observations for both material are realised. Thereafter, novel formulations of cutting force model in milling are developed associated to precise treatment and identification process. Thus, the cutting forces are modelled with a mechanistic approach fully parameterized, and furthermore the tool geometry as well as the local forces model consider tool flank wear effect. This study shows that additive manufactured Inconel 718 has a better machinability and that considering tool wear with tool geometry evolution improves the model precision.

Keywords: Cutting force model; Tool wear; Tool geometrical model; Additive manufactured; Inconel 718

Graphical Abstract:
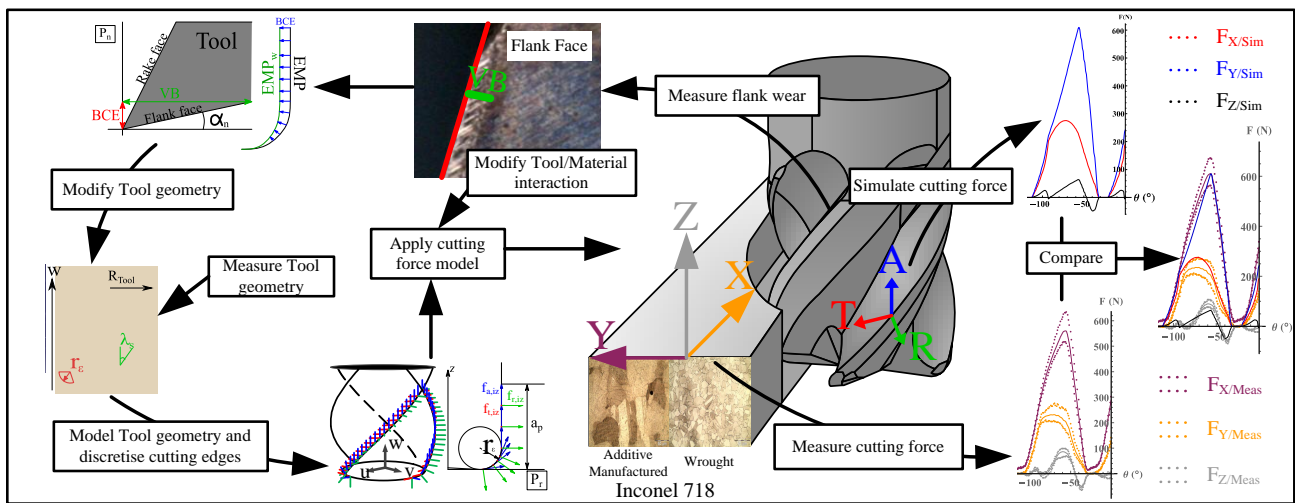
Nomenclature

Frames	
WPF = {O, {$\underline{X}$, $\underline{Y}$, $\underline{Z}$}}	Workpiece Frame
TF = {O_T, {$\underline{u}$, $\underline{v}$, $\underline{w}$}}	Tool Frame
TRA = {O_S, {$\underline{N_{Ps}}$, $\underline{N_{Pr}}$, $\underline{P_s \cap P_r}$}}	Local discretisation Frame where O_s is a point of the cutting edge
NGS = {O_S, {$\underline{N_{Rf}}$, $\underline{N_{Pn}}$, $\underline{R_f \cap P_n}$}}	Local rake face Frame with R_f = Rake face of the tool
Index	
I_{Fl}	i_{Fl}th flute/cutting edge of the tool
i_z	i_zth segment of the cutting edge
i_k	i_kth component of the cutting forces in TRA

i_θ	$i_\theta{}^{th}$ angular position of the rotation angle θ in TF
i_{Tr}	$i_{Tr}{}^{th}$ trial
i_{Co}	$i_{Co}{}^{th}$ component of the cutting forces in WPF

Tool parameters

Z	Number of flutes
R_{Tool}	Tool radius (mm)
r_ε	Corner radius of the tool (mm)
z	Altitude of a cutting edge O_s point in TF (mm)
θ	Rotation angle of the tool in TF (°)
P_r	Normal plane to V_c direction and containing O_S and $\underline{Z_{TF}}$
P_s	Normal plane to P_r and tangent to the cutting edge
P_n	Normal Plane to P_r and P_s and containing O_s
$\Psi[i_{Fl}]$	Differential pitch of the $i_{Fl}{}^{th}$ flute (°)
$\lambda_s[z]$	Helix angle function of z and defined in P_s (°)
a_u	u^{th} Coefficient of the function $\lambda_s[z]$ (mm^{-u})
γ_o	Rake angle of the cutting edge measured in P_o (°)
α_o	Flank angle of the cutting edge measured in P_o (°)

Cutting parameters

V_c	Cutting speed (m.min^{-1})
f_z	Feed (mm.rev^{-1}.tooth^{-1})
a_e	Tool radial engagement (mm)
a_p	Axial depth of cut (mm)
h	Cut thickness (mm)
b	Discretised cutting edge length engaged (mm)
Nb_{seg}	Number of segments for each cutting edge after discretisation

Geometrical objects

$\underline{EMP}[z]$	End Mill Profile
$\underline{TCT}[\theta]$	Tool Centre Trajectory
$\underline{CE_{ref}}[z]$	Reference Cutting Edge
$\underline{CE}[i_{Fl}, z]$	$i_{Fl}{}^{th}$ Cutting Edge
$\underline{R_{out}}[i_{Fl}, z]$	$i_{Fl}{}^{th}$ cutting edge Runout at the altitude z
$\underline{SCE}[i_{Fl}, z, \theta]$	Surface generated by the $i_{Fl}{}^{th}$ flute/cutting edge

$\underline{NV}_{SCE}[i_{Fl}, z, \theta]$	Normal Vector with respect to $\underline{SCE}$

Force components and macroscopic friction coefficient

$\{f_t, f_r, f_a\}_{TRAiz}$	Local forces of the $i_z{}^{th}$ cutting edge segment applied on the workpiece in TRA_{i_z} (N)
$\{F_X, F_Y, F_Z\}_{WPF}$	Global forces of the tool applied on the workpiece in WPF (N)
Cf_{Rake}	Macroscopic friction coefficient on the rake face
Cf_{Flank}	Macroscopic friction coefficient on the flank face

Model Identification/Validation parameters

$Nb_{Tr(Id/Val)}$	Number of Trial for Identification/Validation
$Nb_{\theta(Id/Val)}$	Number of Measured Positions for Identification/Validation
$Nb_{Co(Id/Val)}$	Number of force Components for Identification/Validation
$List\theta Meas$	List of tool angular measured values, from 0 to 360°
$List\theta Id[Nb_{\theta Id}]$	List of $Nb_{\theta Id}$ tool angular values θ used for Identification
$List\theta Val[Nb_{\theta Val}]$	List of $Nb_{\theta Val}$ tool angular values θ used for Validation
$InValue[List\theta Val]$	% of positions from $List\theta Val$ where $\{F_{iCo}^{Min}\}_{Meas/WPF} < \{F_{iCo}\}_{Sim/WPF} < \{F_{iCo}^{Max}\}_{Meas/WPF}$

Operator

$\underline{Rot}_{\underline{A}}[\theta]$	Rotation matrix of angle θ around the axis A

1. Introduction

The high strength for high temperature and the high corrosion resistance of Inconel 718 make it one of the main materials used for hot parts in aero engines. Nevertheless, due to its properties, it is also considered as a hard-to-cut material. In order to limit the machining time, Additive Manufactured (AM) part are more and more produced to get a near net shape before machining operation. Yet, there is a lack of knowledge concerning the machinability of additive manufactured Inconel 718. Wang et al. [1] demonstrates that to ensure good mechanical properties of additive manufactured parts by applying heat treatment. However, AM material has still a lower yield strength and a higher elastic modulus than Wrought (WRT) one. The microstructures of AM parts are widely different and mainly depends on the applied heat treatment after manufacturing according to Chlebus et al. [2]. This may lead to a different machinability than wrought Inconel 718.

Cutting forces are a major concern to perform milling operation with high reliability. Altintas [3] shows that reducing cutting forces leads to restrain vibrations, deformations and improve tool life. Thus, to qualify machinability, the cutting forces analysis is essential. Predictive models help the connection between the global forces on the workpiece and the local interaction of the chip with the cutting edge. Armarego et al. [4] are one of the first to describe both the edge and the cut effect in a unique mechanistic model to determine cutting forces in the case of a tool without helix angle. Edge effect is under influence of the cutting edge preparation and the workpiece contact whereas the cut effect models the effect of the chip formation mechanism. Then, Armarego et al. [5] develop the previous model for end mill cutting geometry using tool discretisation. Kaymakci et al. [6] later generalize this model to all cutting process. In addition to mechanical aspects, the main issues to model cutting forces in milling operation is also to consider all geometrical aspects of the end mill. These aspects are helix angle, differential pitch, radial runout and complex tool envelop. According to Fromentin et al. [7], tools with complex definition affect the cut section over time. In this case, it is required real adapted methodology for the cut thickness determination. Therefore, Killic et al. [8] develop a generalised tool model formulation to optimise the cutting force simulation. Zheng et al. [9] propose a model which takes into account the runout. It substantially improves the accuracy of the simulation as it well computes the actual engagement angle of each cutting edge. Helix angle has also a large influence on the engagement angle of a cutting edge and axial cutting force (F_z). Ozturk et al. [10] study this impact of a variable helix angle to improve machining performance. Niu et al. [11] implement a different helix angle between pairs of cutting edges, a variable pitch and the tool runout in a mechanistic model considering edge and cut effects. Bissey-Breton et al. [12] add the helix angle in the mechanistic model to represent the chip flow direction effect which have a great repercussion on the cutting forces for high helix angle.

Tool wear is a determinant factor for surface integrity and cutting forces. Tool life is excessively reduced in machining Inconel 718 compared to other materials used in aircraft industry such as aluminium alloys. Dudzinski et al. [13] summarise the work done on tool wear mechanism in machining Inconel 718 with carbide tools. They observe a high abrasion on the flank face and notching at the depth of cut. That is why reliable cutting model should be built including tool wear effect. Oraby et al. [14] show the connection between tool wear and cutting forces to implement tool wear in cutting forces model for turning operation. Li et al. [15] also develop a model considering the effect of reduced lubrication to analyse the influence of tool wear on the friction coefficient between the chip and the cutting edge. Then, Sun et al. [16] use flank wear measurement implemented in a cutting forces model in end milling operation of Ti6Al4V. Nevertheless, these models only have considered the tool wear as a modification of the cutting process with an interaction between the chip and the cutting edge by implementing a term in their cutting forces law. The tool wear has also an impact on the tool geometry itself [13, 15, 16]. Indeed the flank wear induces an edge recoil which leads to a modification of the cutting edge engagement [11]. Thus, the tool wear should be included in both tool geometry and cutting forces model.

4

Consequently, the machinability of AM Inconel 718 should be studied relative to microstructure changes, cutting forces and tool wear mechanism. Mechanistic model for cutting forces needs to include the most precisely possible tool wear considering the tool geometry modification and the contact interaction evolution. Based novel approaches, the present study will focus on these aspects, clearly highlight the processes of force treatment, model identification in milling and propose a way for analysis modelling precision.

2. Experimental materials

2.1. AM and WRT work materials

Both AM and WRT Inconel 718 are machined in this study. The AM parts are based on a laser melting of powder. It is the Direct Metal Laser Solidification (DMLS) process, which is based on melting a layer of powder and constructing a 3D piece layer by layer. The results of hardness measurements in both materials are shown in Fig. 1. For AM parts, the hardness is measured in the printed direction (different planes) and in the transversal direction (same planes a plane is too thin to be measured independently). The hardness machine has previously been adjusted on a material standard with a certified hardness equal of 50 HRC and a measurement trueness of ±1 HRC is observed.

The mean hardness measured is 44.7 HRC for AM material in the printed direction, is 44.6 HRC for AM material in the transversal direction and is 44.3 HRC for WRT material. All results show a hardness variation within the measurement trueness of the machine (±1 HRC). Hence, no visible difference between both materials in term of macroscopic hardness can be observed due to the resolution of the measuring system. Moreover, the AM parts have no difference either in macroscopic hardness regarding the print and the transversal direction.
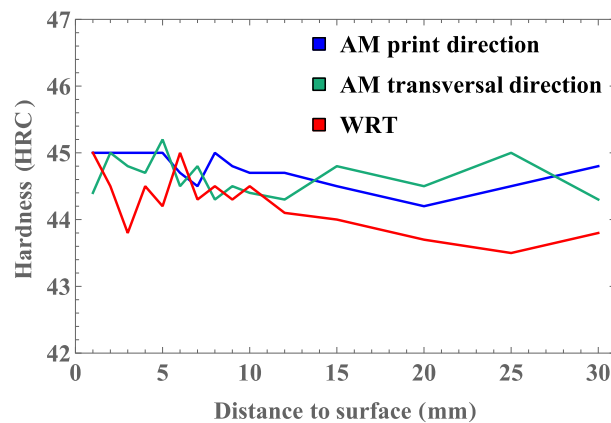

Fig. 1 Comparison of hardness for AM and WRT materials

Both materials are heat treated to obtain quite similar global mechanical properties. The heat treatment is designed to eliminate anisotropic structure, laves, lack of density and other defects of AM processed material. Their chemical compositions are presented in Table 1.

Table 1. Chemical composition for AM and WRT Inconel 718 (wt%).

Material	Ni	Cr	Fe	Nb	Mo	Ti	Al	Co
AM	52.4	18.6	17	5	3	1	0.5	1
WRT	52	19	17	5.1	3.1	1	0.5	1

According to Pan et al. [17], Inconel 718 strength is largely due to the γ'-Ni$_3$Nb and the γ''-Ni$_3$(Al,Ti) precipitates. Concerning the microstructure, Kamdar [18] explains that a large typical grain size limits the nucleation of cracks whereas a small one limits the propagation of cracks. Indeed, grain boundaries form obstacles for the dislocation movements and so the cracks propagations. As machining is based on crack propagation along the cutting edge to create a chip, the smaller the grain size is, the harder-to-cut the material will be. The microstructures of AM and WRT studied materials are presented in Fig. 2. During microstructure observation, no anisotropy has been observed on AM parts. The grain size is evaluated according to the standardised method in ASTM E112-13 [19], the carbide size and the twin grains frequency are visually estimated on a 9 mm^2 sample. The results are given in Table 2. The grain size of AM material is about thirty times larger than the WRT one. Therefore, the crack propagation is much more limited in WRT material because of all grains boundaries. Both materials have high frequency of twin grains. This characteristic is also a barrier to the dislocation movement.
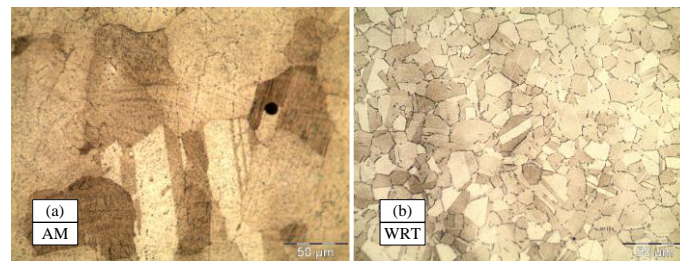

Fig. 2. Inconel 718 (a) AM and (b) WRT microstructure before machining.

Table 2. Microstructure analysis of Inconel 718 before machining.

Material	Grain size (G)	Carbide density with AZtec (mm^{-2})	Twin grains
AM	6.63	43	Frequent
WRT	9.21	68	Frequent

High proportion of Niobium favours the formation of Niobium carbides (NbC) which are highly resistant at cutting temperatures (between 800°C and 1000°C). According to Karasev et al. [20], other carbonitrides such as TiCN and (Nb,Ti)CN are also present in the Inconel 718 microstructure. Inclusions size and density for both materials are evaluated using SEM-EDS combined with AZtec software. Values of Equivalent Circular Diameter (ECD) are presented in Fig. 3. In the present study, these three types of carbides are analysed: NbC, TiCN and (Nb,Ti)CN. By this analysis it is shown that WRT material presents the largest carbides for all types analysed. Moreover, as seen in Table 2, WRT material presents also the highest density of carbides.
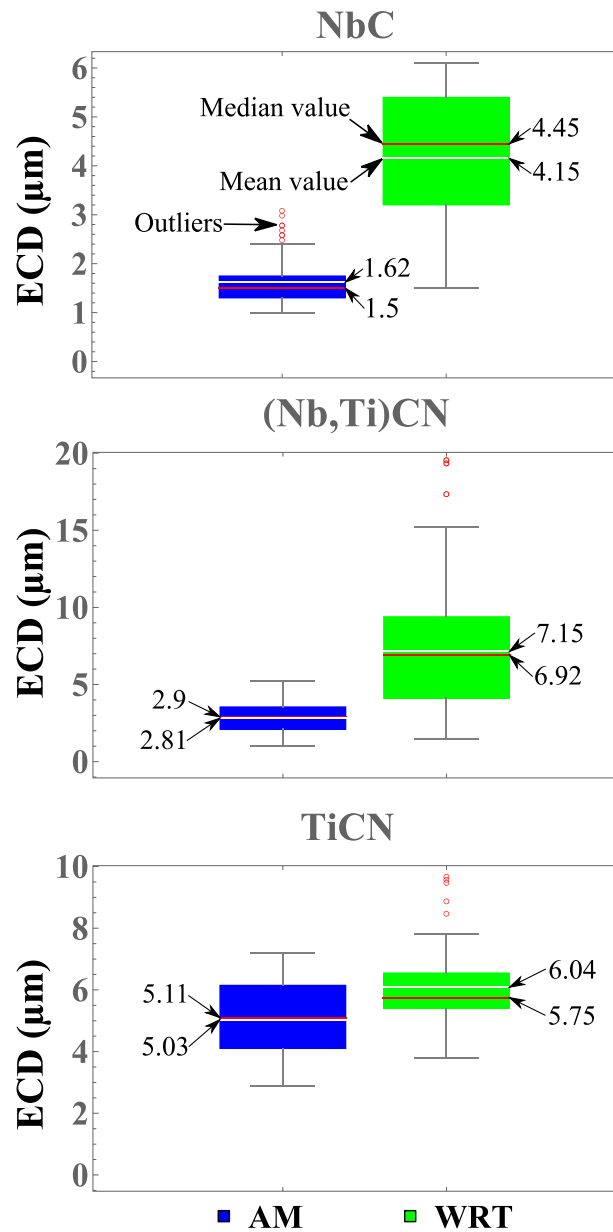
Fig. 3 Carbides size (ECD) distribution measure using SEM-EDS and Aztec software.

Carbide size may be a sensitive indicator to evaluate machinability. Carbide is very difficult to cut during machining. Three different options would happen according to Dudzinski et al. [13]. Firstly, the carbide is cut and so high cutting forces are locally generated on the cutting edge. Secondly, if the carbide is small enough, the tool tears off the carbide from the material and will create a hole at the machined surface. Otherwise, the carbide is not cut and damages the tool by flank surface scratching. As the carbides of WRT material are larger than the AM material one, they are more likely to damage the tool than to be torn off. Consequently, WRT material may locally generate greater cutting forces and bigger scratch on the cutting edges compare with AM material.

2.2. Tool analysis and modelling

During this study, the used tools are solid coated carbide end milling cutters with four flutes and corner radius from Mitsubishi Materials (IMX10C4HV100R10010S EP7020). The tool parameters are shown in Table 3. In order to evaluate all parameters, the tool is scanned using an Alicona InfiniteFocusSL which

generates a cloud of points. After post-processing in a CAD software to build the flank and rake face along the cutting edges, actual tool parameters can be measured and results are depicted in Fig. 4.

Table 3. Measured tool parameters

Coating	R_{Tool} (mm)	r_ε (mm)	Z	Ψ (°)	γ_o (°)	α_o (°)	r_β (µm)
(Al,Cr)N (2µm)	5	1	4	{0, 2, 0, 2}	6	6	3 - 4

The global tool parameters (i.e. R_{Tool} and r_ε) are used for defining the End Mill Profile (EMP) towards the point height z in the tool frame TF. This tool design presents both a variable helix angle along the cutting edge and a variable pitch Ψ. The local cutting angles (λ_s, γ_o, α_o) are evaluated along the cutting edge using the ISO 3002-1:1982 [21] and computed as function of the height z of a cutting edge point. The flank and rake angles are measured as constant along the cutting edge. Finally, the angle λ_s is described by a sum of piecewise continuous third degree polynomial functions which is $\mathcal{C}^2(\mathbb{R};\mathbb{R})$ between two points every 0.1 mm as presented in Fig. 4.
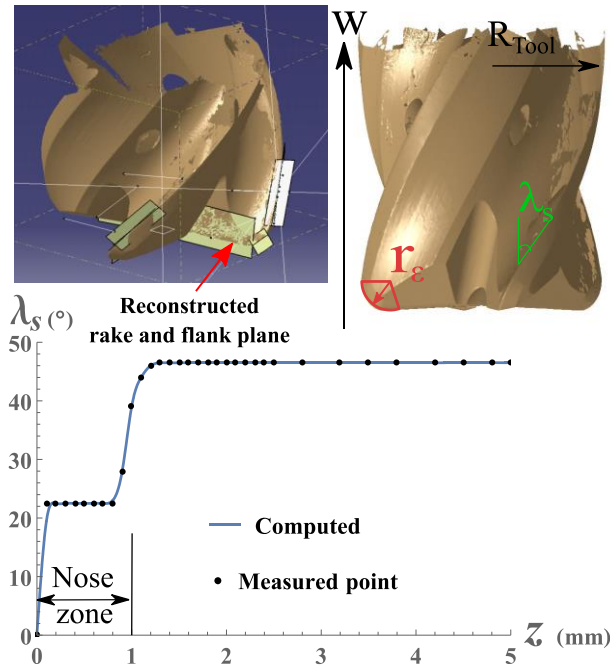

Fig. 4. Tool scan and helix angle λ_s evolution along cutting edge.

Due to a great influence of runout on the engagement angle and the cut thickness (h) along each cutting edge, the radial runout should be examined. Therefore, an in-situ scan of the tool is performed with a laser profilometer Keyence LJV7060. The radial runout R_{out} of the i_{Fl}^{th} cutting edge is computed as an update of the tool radius for this edge considering the runout at the altitude z. From EMP and λ_s, the Reference Cutting Edge $\underline{CE}_{ref}$ is modelled in TF by Eq (1) considering the radial component of $\underline{EMP}$ noted EMP_r, the axial wich is equal to z and the radial runout R_{out}.

$$\left\{ \underline{CE_{ref}}[i_{Fl},z]\right\}_{TF} = \left\{ \begin{array}{l} (EMP_r[z] + R_{out}[i_{Fl},z]) * \cos\left(\dfrac{z * \tan(\lambda_s[z])}{EMP_r[z] + R_{out}[i_{Fl},z]}\right) \\[3mm] (EMP_r[z] + R_{out}[i_{Fl},z]) * \sin\left(\dfrac{z * \tan(\lambda_s[z])}{EMP_r[z] + R_{out}[i_{Fl},z]}\right) \\[3mm] z \end{array} \right\}_{TF} \tag{1}$$

$$where\ \lambda_s[z] = \sum_{u=0}^{3} a_u * z^i$$

Finally, all cutting edges are developed from Eq. (1) considering measured differential pitch Ψ following Eq (2).

$$\left\{ \underline{CE}[i_{Fl},z]\right\}_{TF} = \underline{\underline{Rot_w}}\left[\frac{2\pi}{Z}(i_{Fl}-1) + \Psi[i_{Fl}]\right] . \underbrace{\left\{ \underline{CE_{ref}}[i_{Fl},z]\right\}_{TF}}_{Eq.(1)} \tag{2}$$

In this way, the geometrical model of the tool considers variable pitches, the progressive helix angle along corner radius and the radial runout of each cutting edge.

2.3. Experimental set-up

Experiments are performed on a Mikron HSM600U 5-axis milling machine equipped by an Heidenhain's iTNC530 CNC. The Fig. 5 represents the sample in the machine with both the tool frame TF, which is in rotation considering the spindle rotation by a θ angle, and the workpiece frame (WPF). The cutting forces are recorded using a Kistler 9119AA2 piezoelectric dynamometer with a sampling frequency of 50 kHz. The tool is attached in a BIG tool holder to limit the maximal radial runout below 20 μm. Finally, a standard 6% emulsion oil is used during machining. The studied configuration (Fig. 5) is a side milling operation in the – X_{WPF} way. The angle θ is recorded, from spindle encoder using a Heidenhain's IBV606 derivation box, with a resolution of 0.17° (256 toothed wheel by twice interpolator by quadrature factor over 360°), and synchronized with force measurements. The trigonometric function θ is decreasing over time, from 0 to -2π in one revolution as the spindle rotates in clockwise direction. According to the derivation box resolution, a list of tool angular measured values ListθMeas is built from 0° to -360° which represents all angular position where a measure is acquired. The tool angular measured value insured no signal shift between experiments and simulations towards time and the trials, which avoid any magnitude effect on model identification. After the initial experimental identification of the tool angular origin, no angular shift is introduced in the modelling process.
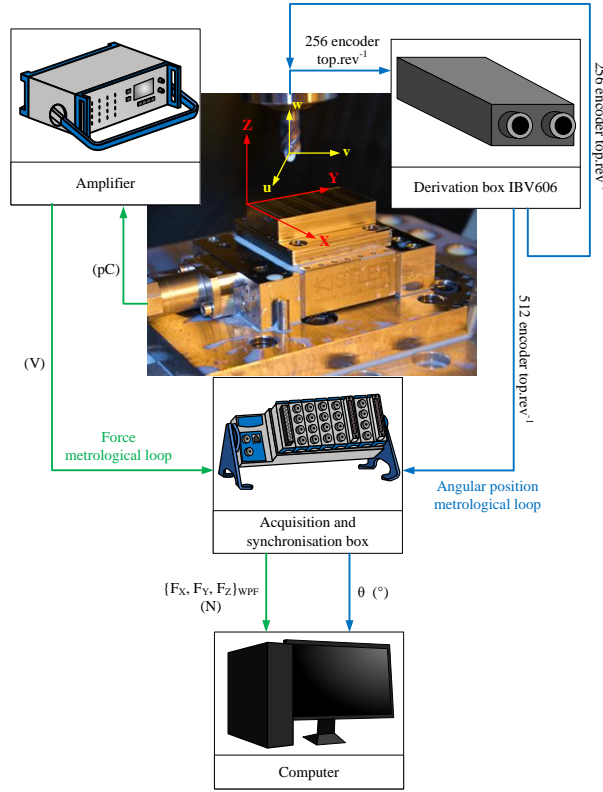
Fig. 5. Machining and measurement set-up.

The optimal cutting parameters are investigated with the tool-material pair process. The cutting speed V_c and the maximal depth of cut a_p are set respectively at 40 m.min^{-1} and at 4 mm.

The tool wear is measured through image analysis taken by a Dino-Lite Edge microscope. The flank wear VB is measured according to ISO 8688-2:1989 [23] along the cutting edge for z from 0 to the axial depth of cut a_p.

3. Mechanistic cutting force model

3.1. Geometrical parametrisation and cut area

The modelling approach is based on a mechanistic model and the cutting edge discretisation methodology. Thereafter, linear milling operation is parametrized, including the full definition of the milling cutter geometry, its runout and the precise computation of the cut thickness h, needed to model local cutting forces.

Considering the feed f_z and the number of flutes Z, the tool centre trajectory TCT, for a straight milling operation into –X way, is evaluate in WPF as a function of spindle angle θ by the following Eq. (3):

$$\{\underline{TCT}[\theta]\}_{WPF} = \begin{Bmatrix} f_z.Z.\dfrac{\theta}{2\pi} \\ 0 \\ 0 \end{Bmatrix}_{WPF} \tag{3}$$

Then, from the end mill rotation, the i_{Fl}th cutting edge definition from Eq. (2) and TCT, the i_{Fl}th cutting edge trajectory S_{CE} is computed in WPF by the Eq. (4) as follows.

$$\{\underline{SCE}[i_{Fl},z,\theta]\}_{WPF} = \{\underline{TCT}[\theta]\}_{WPF} + \underline{Rot_Z}[\theta].\{\underline{CE}[i_{Fl},z]\}_{TF} \tag{4}$$

10

Based on this parametrisation, the cut thickness h is determined by solving numerically its real formulation [7]. That means, in this study no approximation is made during the three steps, which are, the cutting edge definition, the surface generated by cutting edges, along their trajectories, and finally the cut thickness computation approach.

Considering the surface $\underline{SCE}$ of the i_{Fl}th edge, the cut thickness h is the normal distance between this surface and the previous surface generated by the $(i_{Fl}-1)$th edge. Thus by geometrical construction in WPF of the unit normal vector $\underline{NV}_{SCE}$ to $\underline{SCE}$, h is determined by finding the intersection between the line defined by $\underline{NV}_{SCE}$ at the i_{Fl}th edge point and $\underline{SCE}$ of the $(i_{Fl}-1)$th edge. It is the solution of Eq. (5) at a tool angular position θ_0 near $\theta+(2\pi/Z)$ and a height z_0 near z.

$$\begin{cases} \underline{SCE}[i_{Fl}-1, z_0, \theta_0] = \underline{SCE}[i_{Fl}, z, \theta] + h[i_{Fl}, z, \theta].\underline{NV}_{SCE}[i_{Fl}, z, \theta] \\ \qquad \theta_0 \approx \theta + \dfrac{2\pi}{Z} \ and \ z_0 \approx z \end{cases} \qquad (5)$$

The cut thickness computation has to be restricted to the positions for θ values where the cutting edges are engaged into work material as presented in Fig. 6; the geometrical conditions are expressed by Eq. (6). In order to reduce computation time, it is processed in the following order. Firstly, if a point M_1 of the cutting edge is at a z higher than the a_p depth of cut, this point is not cutting, so h is directly set to 0. Secondly, considering the projection of a M_2 point on $\underline{SCE}[i_{Fl}]$, on the orthogonal axis Y_{WPF} to the feed direction $\underline{X}$, if its ordinate is lower than the parameter $EMP_r[z]-a_e$, this M_2 cutting edge point is actually not in work piece, then h is also set to 0. Thirdly, if a point M_3 of the $\underline{SCE}$ on backside from feed direction, the cut thickness h calculated is negative according to Eq (5), the value is replaced by 0. Finally, in any other case (i.e. in the work zone), h solution computed according to Eq. (5) is valid.
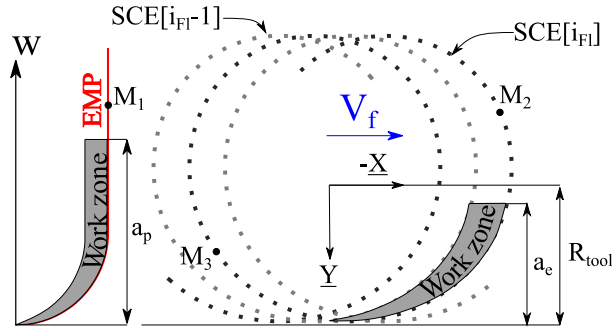

Fig. 6. Cut thickness limitation zones.

$$\begin{cases} \qquad If \ z[M_1] > a_p, M_1 \ is \ a \ point \ where \ h = 0 \\ If \ \underline{SCE}[M_2].\underline{Y}_{WPF} < EMP_r[z] - a_e, M_2 \ is \ a \ point \ where \ h = 0 \\ \qquad If \ h[M_3] < 0, M_3 \ is \ a \ point \ where \ h = 0 \end{cases} \qquad (6)$$

3.2. Cutting force simulation and measurement treatment

3.2.1. Cutting force simulation
During this study, in order to deal with the complex geometrical problem, the modelling approach is based on the edge discretization methodology. The tool is divided along the cutting edge every 0.025 mm in the nose radius and every 0.05 mm in the lateral edge towards z altitude. The cutting mechanics is modelled with using

a mechanistic approach. Therefore, it is proposed to model local cutting forces $\{f_t, f_r, f_a\}$ in TRA frame as defined by Eq. (7):

$$
\begin{aligned}
\{f_t[i_{Fl},\theta]\}_{TRA_{iz}} &= b_{iz}\left(\underbrace{K_{tb}}_{Edge\,effect} + \underbrace{K_{th}.h_{iz}[i_{Fl},\theta]}_{Cut\,effect}\right)\left(\underbrace{1 + K_{t\lambda}.\lambda_{s\,iz}}_{Chip\,flow\,effect}\right) \\[2mm]
\{f_r[i_{Fl},\theta]\}_{TRA_{iz}} &= b_{iz}\left(\underbrace{K_{rb}}_{Edge\,effect} + \underbrace{K_{rh}.h_{iz}[i_{Fl},\theta]}_{Cut\,effect}\right)(\underbrace{1 + K_{r\lambda}.\lambda_{s\,iz}}_{Chip\,flow\,effect}) \\[2mm]
\{f_a[i_{Fl},\theta]\}_{TRA_{iz}} &= b_{iz}\left(\underbrace{K_{ab}}_{Edge\,effect} + \underbrace{K_{ah}.h_{iz}[i_{Fl},\theta]}_{Cut\,effect}\right).\underbrace{\lambda_{s\,iz}}_{Chip\,flow\,effect}
\end{aligned}
\qquad (7)
$$

This cutting law can be modelled as the combination of three effects. The first and the second are the edge effect ($b_{iz}*K_{ikb}$) and the cut effect ($b_{iz}*K_{ikh}*h_{iz}$) where $i_k \in \{t,r,a\}$ presented by Armarego et al. [4]. The last one is the effect chip flow direction described by Bissey-Breton et al. [12] which depends on the local helix angle, it is the cutting edge obliquity effect. This effect influences the edge effect as the helix angle modifies the apparent cut angle in P_r plane. Moreover, it modifies the chip flow direction and so the friction direction between the chip and the tool. That is why it impacts also the cut effect. The model coefficients K_{ikb}, K_{ikh} and $K_{ik\lambda}$, where $i_k \in \{t,r,a\}$, are later identified from cutting force measurement in WPF.

The complete process for cutting forces simulation is explained in Fig. 7. Once obtaining $\{f_t, f_r, f_a\}_{TRA}$, they are expressed in TF using the transfer matrix $M_{TF\leftarrow TRA_{iz}}$. Then, the global cutting forces $\{F_X, F_Y, F_Z\}_{TF}$ in TF are obtained by summing the local ones from every segments (Nb_{seg}) and on every teeth (Z). Finally, with the transfer matrix $M_{WPF\leftarrow TF}[\theta]$ the global forces are determined in WPF.
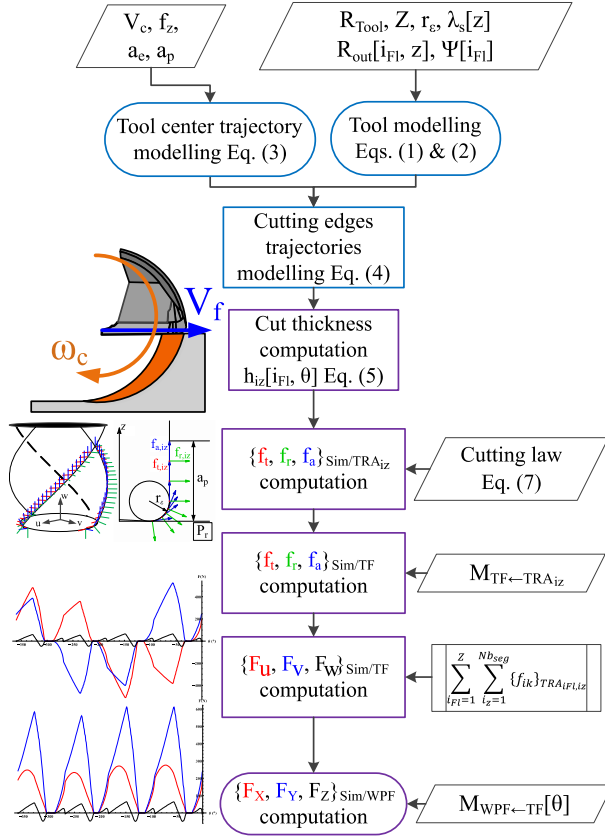
Fig. 7. Computation algorithm of cutting forces in workpiece frame.

3.2.2. Cutting force measurement and treatment

The complete measurement treatment is presented in Fig. 8. Thank to spindle encoder position, it includes filtering and averaging over tool angular position for characterising precisely cutting force variation towards tool revolutions.

The global cutting forces are recorded in WPF (cf. section 2.3). Force signals are only analysed during the steady state, i.e. tool fully engaged into workpiece, which stands for approximatively 40 revolutions. The time based recorded forces for multiple revolutions are evaluated towards θ measurements from ListθMeas and superimpose on a one angular revolution base. Then, in order to eliminate the noise on the signals over time or angular position, a moving average filter with 31 values is applied all along the recording data. Finally, based on 40 revolutions signals, i.e. 40 values for any tool angular position, three representative curves are computed from the measurement for each of the three force components in WPF. The $\overline{F_{iCo}}$, with $i_{Co} \in \{X,Y,Z\}$, which describes the mean of the measured values at the i_θ^{th} position from ListθMeas, the F_{iCo}^{Min} and F_{iCo}^{Max} which respectively describes the minimum and the maximum measured value at the i_θ^{th} position from ListθMeas. As a consequence, these representative curves characterise the natural fluctuations of force components over multiple tool revolution, and a model precision has to be analysed in the light of them.
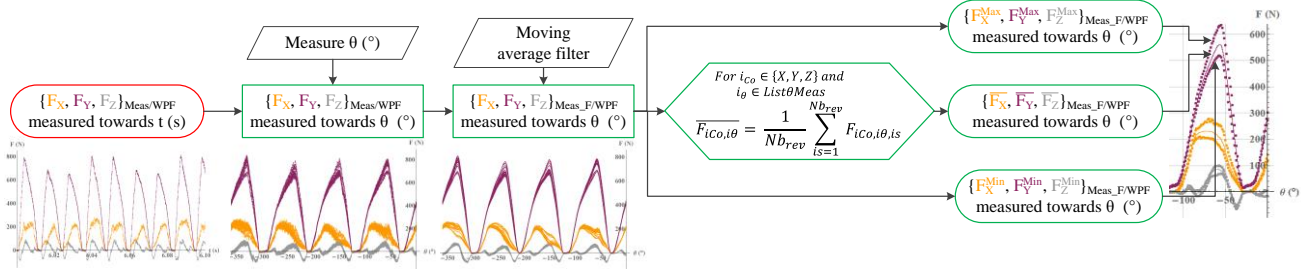
Fig. 8. Cutting forces measurement treatment.

In the following, only treated cutting forces, i.e. representative curves (last stage of treatment in Fig. 8), are used so the notation $\{\overline{F_{iCo}}\}_{Meas\_F/WPF}$ is equal to $\{\overline{F_{iCo}}\}_{Meas/WPF}$ with $i_{Co} \in \{X,Y,Z\}$. The same notation is used for $\{F_{iCo}^{Min}\}_{Meas/WPF}$ and $\{F_{iCo}^{Max}\}_{Meas/WPF}$.

3.3. Cutting force model identification and validation method

An inverse identification is carried out to determine the coefficients K_{ikb}, K_{ikh} and $K_{ik\lambda}$, $i_k \in \{t,r,a\}$, of cutting laws i.e. Eq. (7). This process of inverse identification is described in Fig. 9. The principle is to simulate cutting forces with unknown coefficients and to establish a set of equations with the relative error towards $\overline{F_{iCo}}$ for a list ListθId of tool angular position composed of Nb$_{\theta Id}$ values. This list excludes the positions where simulated cutting forces are nulls. It ensures that no equation is going to identify a noise kept from the measurements. Furthermore, no angular delay is introduced over time or the trials in order to fit the simulations with the experiments; the process is deterministic concerning this aspect thank to the measurement of spindle angular position in a reliable way. Then, the error sum ε of related to all directions and all trials, from 1 to respectively Nb$_{Co}$ and Nb$_{Tr}$, is minimised using Levenberg-Marquardt algorithm by adjusting the coefficients of Eq. (7). The number Nb$_{Co}$ is equal to 3 reflecting $i_{Co} \in \{X,Y,Z\}$. The number Nb$_{Tr}$ is equal to the number of used trial for identification. It corresponds to the Id index in the column Usage in Table 5. In the system equations, the number of them is the product of Nb$_{TrId}$, Nb$_{\theta Id}$ and Nb$_{Co}$. Then, residual degree of freedom (RDOF) is equal to 3* Nb$_{TrId}$* Nb$_{\theta Id}$ -9, because of 9 coefficients K_{kb}, K_{kh} and $K_{k\lambda}$, $i_k \in \{t,r,a\}$ are determined in Eq (7). A high RDOF insure a robust determination of the model. Nevertheless high RDOF leads to solve many equations. As consequence, the trials and the list of angular position ListθId for identification have to be carefully selected.
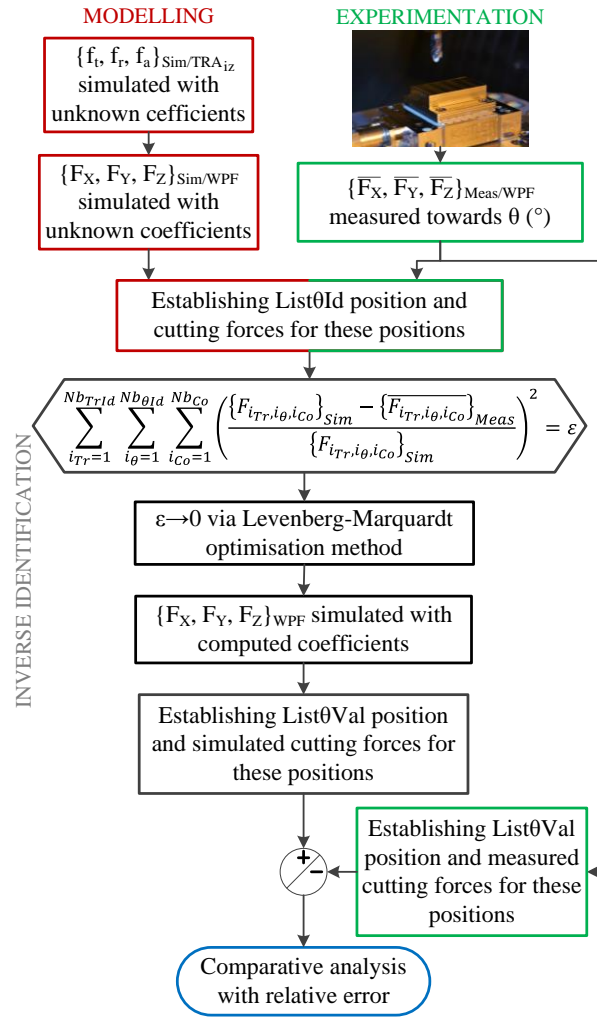
Fig. 9. Cutting forces simulation and inverse identification process.

The identified coefficients, presented in Table 4, are then implemented in the simulation process to get the global cutting forces $\{F_{iCo}\}_{\text{Sim/WPF}}$. Then a comparative analysis with $\{\overline{F_{iCo}}\}_{\text{Meas/WPF}}$ is performed to validate the fitness of purpose. The complete trials used for validation (Val index) trials are given in Table 5 for fresh tool.

Table 4. Cutting law coefficients in TRA for fresh and worn tool.

Cutting law coefficient	For WRT material		For AM material	
	Fresh tool	Used tool	Fresh tool	Used tool
K_{tb} (N/mm)	73 – 84	72 – 101	54 – 61	55 – 75
K_{tw} (MPa)		9 – 10		9 – 10
K_{th} (MPa)	3312 – 3488	3289 – 3401	3154 – 3281	3109 – 3245
$K_{t\lambda}$ (%/°)	0.09	0.09	0.09	0.09
K_{rb} (N/mm)	41 – 63	36 – 61	51 – 73	51 – 78
K_{rw} (MPa)		11 – 13		11 – 12
K_{rh} (MPa)	754 – 796	748 – 788	674 – 708	701 – 726
$K_{r\lambda}$ (%/°)	0.1 – 0.3	0.1 – 0.3	0.8 – 1.3	0.8 – 1.5

15

K_{ab} (N/mm/°)	$0.3 - 0.6$	$0.3 - 1$	$0.3 - 0.5$	$0.3 - 0.5$
K_{aw} (MPa)		$0.2 - 0.3$		$0.1 - 0.2$
K_{ah} (MPa/°)	$17.5 - 22.8$	$20.5 - 22.8$	$18.2 - 21.9$	$18.1 - 21.4$

The identification has been done on a reduce set of position defined by ListθId, so as to reduce computation time. Nonetheless the validation may be easily analysed on much more tool angular values, ListθVal. Eventually, if there is a teeth cutting continuity, it may be validated on any measured tool angular values, i.e. on ListθMeas. If not, validation would deal with angular positions with null simulated force and pure experimental noise on the measured force. That's make no sense in term of modelling error.

Based on these considerations, the validation approach is the following. From ListθMeas a list of θ angular position with one point each degree is set. Then, every angular positions, where $\{F_{iCo}\}_{\text{Sim/WPF}}$ is lower than 10% of the maximal simulated forces along $i_{Co} \in \{X,Y,Z\}$ direction for all positions, are taken back from this list to establish ListθVal. The length of ListθVal is $Nb_{\theta Val}$. Then, at the positions from ListθVal, the absolute gap between $\{F_{iCo}^{Min}\}_{\text{Meas/WPF}}$ and $\{F_{iCo}^{Max}\}_{\text{Meas/WPF}}$ for each direction in WPF is calculated with Eq. (8), it represents the experimental force variation over tool revolutions. Finally, the absolute error between simulated and mean measured cutting forces with Eq. (9) considering $i_{Co} \in \{X,Y,Z\}$. The results are presented in Table 5 for fresh tool.

$$\Delta F_{iCo} = \sqrt{\frac{1}{Nb_{\theta Val}.Nb_{TrVal}} \sum_{iTr=1}^{Nb_{TrVal}} \sum_{i\theta=1}^{Nb_{\theta Val}} \left(\{F_{i_{Tr},i_\theta,i_{Co}}^{Max}\}_{Meas/WPF} - \{F_{i_{Tr},i_\theta,i_{Co}}^{Min}\}_{Meas/WPF} \right)^2} \tag{8}$$

$$Error_{iCo} = \sqrt{\frac{1}{Nb_{\theta Val}.Nb_{TrVal}} \sum_{iTr=1}^{Nb_{TrVal}} \sum_{i\theta=1}^{Nb_{\theta Val}} \left(\{F_{i_{Tr},i_\theta,i_{Co}}\}_{Sim/WPF} - \{\overline{F_{i_{Tr},i_\theta,i_{Co}}}\}_{Meas/WPF} \right)^2} \tag{9}$$

Finally, the relative error towards all directions is given by Eq. (10):

$$Error_{XYZ} = \sqrt{\frac{1}{Nb_{\theta Val}.Nb_{TrVal}.Nb_{Co}} \sum_{iTr=1}^{Nb_{TrVal}} \sum_{i\theta=1}^{Nb_{\theta Val}} \sum_{iCo=1}^{Nb_{Co}} \left(\frac{\{F_{i_{Tr},i_\theta,i_{Co}}\}_{Sim/WPF} - \{\overline{F_{i_{Tr},i_\theta,i_{Co}}}\}_{Meas/WPF}}{\{F_{i_{Tr},i_\theta,i_{Co}}\}_{Meas/WPF}} \right)^2} \tag{10}$$

The result is also given for the fresh tool model in Table 5. A final validation is done by computing the InValue which represents the percentage of positions from ListθVal included in the experimental pipe, that means where $\{F_{iCo}\}_{\text{Sim/WPF}}$ is greater than $\{F_{iCo}^{Min}\}_{\text{Meas/WPF}}$ and lower than $\{F_{iCo}^{Max}\}_{\text{Meas/WPF}}$ for all directions $i_{Co} \in \{X,Y,Z\}$ (i.e. $\forall i_{Co} \in \{X,Y,Z\}$ and $\forall \theta \in$ ListθVal, $\{F_{iCo}^{Min}[\theta]\}_{\text{Meas/WPF}} < \{F_{iCo}[\theta]\}_{\text{Sim}} < \{F_{iCo}^{Max}[\theta]\}_{\text{Meas/WPF}}$).

3.4. Cutting force model analysis for fresh tool

3.4.1. Cutting force analysis

The model for fresh tool presented in Eq. (7) is identified with trials in Table 5. The cutting conditions choice covers multiple configurations such as teeth cutting continuity and discontinuity or only nose radius work ($a_p = r_\varepsilon = 1$ mm). The identified coefficients are given in Table 4. The variation proposed for coefficients correspond to different tested tools. It appears small variations in local tool geometries such as the rounded

cutting edge radius r_β can lead to variation of the edge effect. Concerning the cut effect variation, according to [24] it may be due to the bond between the coating and the tool material. Furthermore, the identification process admits certain uncertainty by the choice of positions in ListθId. Some of the tested conditions results are shown in Fig. 10.
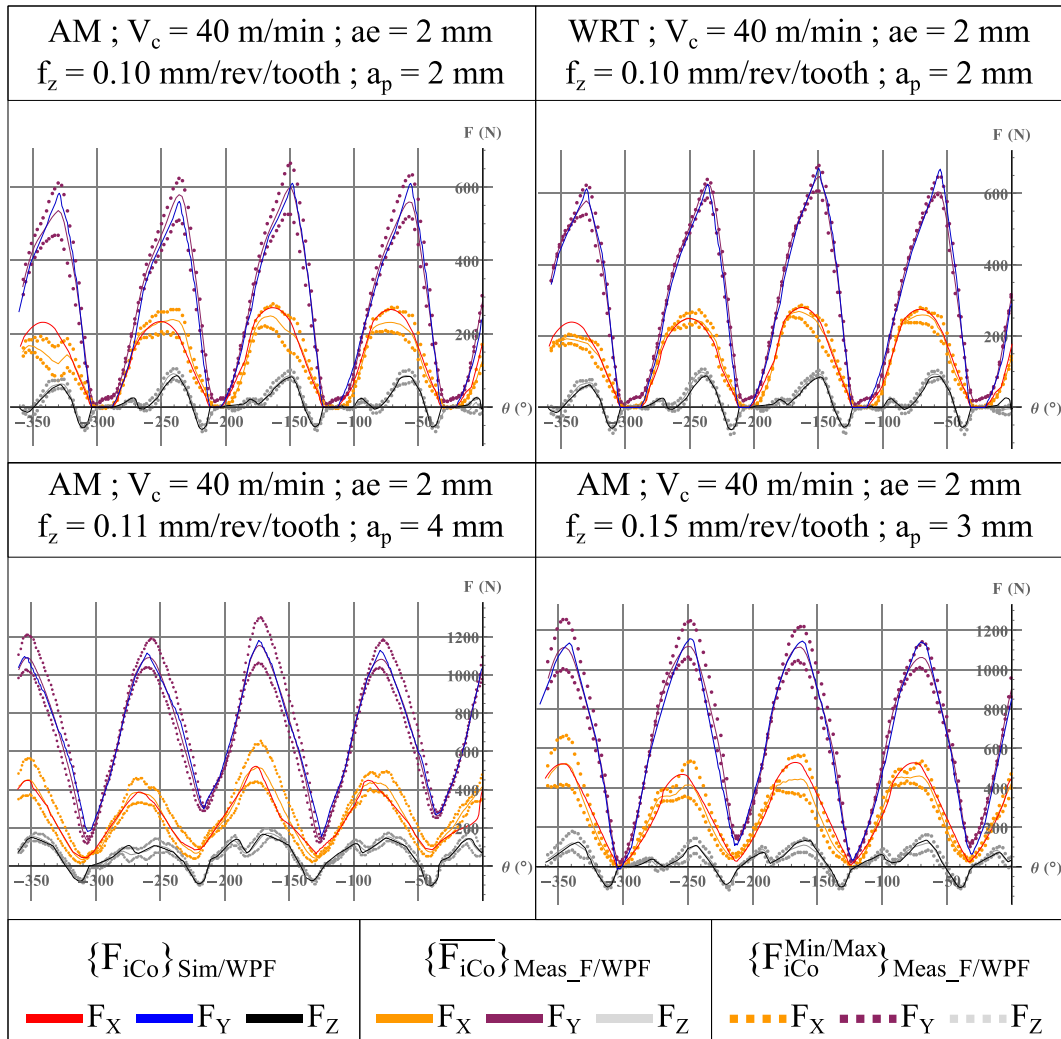

Fig. 10. Cutting forces simulated and measured for fresh tool.

In Fig. 10, a difficulty to model the cutting edge exit can be seen. It is due to a formation of a build-up edge which friction and so cutting force at this location.

3.4.2. Model coefficients analysis

Firstly, the machined material has a limited impact on the chip flow effect. Indeed, the identified coefficients are similar in all directions in TRA. To analyse the identified coefficients, the macroscopic friction coefficient can be determined using force components projected from frame TRA to frame NGS as shown in Fig. 11.
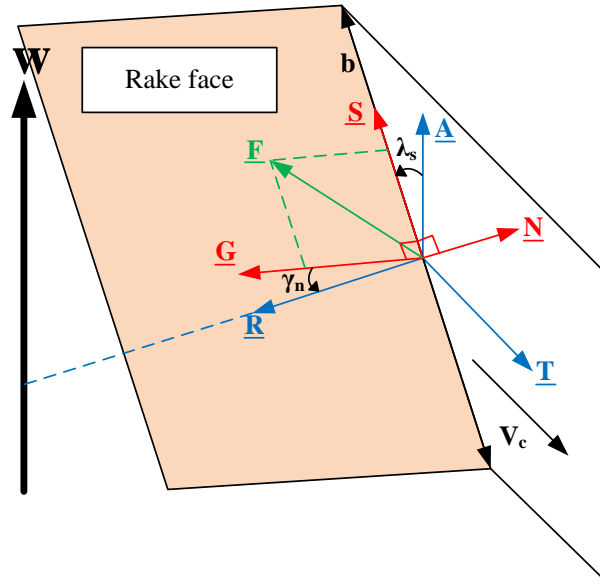
Fig. 11. Rake face projection from TRA to NGS.

By this way the ratio of the normal force of the edge along $\underline{N}$ and the tangential one along $\underline{F}$ on the rake face is equal to a macroscopic friction coefficient Cf_{Rake}. Hence, the coefficient Cf_{Rake} for WRT is equal to 0.63 and is 6% higher than the AM one along the cutting edge.

Concerning the edge effect, the direction of friction velocity between the workpiece and the flute is along V_c direction as seen in Fig. 11. Thus, the friction on the flank face is opposite to $\underline{T}$ direction. The macroscopic friction coefficient Cf_{Flank} on this face is computed as the ratio of the cutting force along $\underline{R}$ and the one along $\underline{V}$ which is the plane $(\underline{T},\underline{A})$. The coefficient for WRT is equal to 1.45 whereas it is equal to 0.71. This coefficient Cf_{Flank} represents the friction on the flank face and also the required energy to form the chip. That is why it can be superior to 1. Finally, the edge has no effect towards the axial direction in TRA.

These two coefficients show that WRT material is more difficult to cut than AM one according to the identified coefficient K_{ikb}, K_{ikh} and $K_{ik\lambda}$, $i_k \in \{t,r,a\}$.

3.4.3. Model Validation analysis

The absolute error of the model $Error_{iCo}$ (according to Eq. (9)) towards each direction and for each material is always lower than the absolute gap ΔF_{iCo} (defined by Eq. (8)) for the same direction and the same material. Correlated with the InValue near 80%, which means that the prediction $\{F_{iCo}\}_{Sim}$ is 80% of the time between $\{F_{iCo}^{Min}\}_{Meas/WPF}$ and $\{F_{iCo}^{Max}\}_{Meas/WPF}$ measures. Finally, the relative error $Error_{XYZ}$ is below the common criteria of 10 %. Hence, the model is valid on the tested cutting conditions domain.

Table 5. Identification and validation trials for mechanistic model with fresh tool.

N° Trial	Usage	V_c (m/min)	f_z (mm/rev/tooth)	a_e (mm)	a_p (mm)
1	Id/Val	40	0.07	2	2
2	Id/Val	40	0.10	2	2
3	Id/Val	40	0.15	2	2
4	Id/Val	40	0.13	3	2
5	Id/Val	40	0.11	3	2.5
6	Id/Val	40	0.15	1	3
7	Id/Val	40	0.30	2	2
8	Id/Val	40	0.13	2	1
9	Val	40	0.11	2	4
10	Val	40	0.11	4	2
11	Val	40	0.08	1	4

	12	Val		40		0.15		2	3
	ΔF$_X$ (N)	Error$_X$ (N)	ΔF$_Y$ (N)	Error$_Y$ (N)	ΔF$_Z$ (N)	Error$_Z$ (N)	Error$_{XYZ}$ (%)	InValue (%)	
WRT	75	53	88	57	32	12	4.2	80	
AM	67	49	73	62	28	16	4.1	82	

	ΔF$_X$ (N)	Error$_X$ (N)	ΔF$_Y$ (N)	Error$_Y$ (N)	ΔF$_Z$ (N)	Error$_Z$ (N)	Error$_{XYZ}$ (%)	InValue (%)

4. Modelling of cutting forces including tool wear

4.1. Tool wear analysis and effects

The tool wear is investigated for WRT and AM Inconel 718 in two different configurations which are presented in Table 6. The objective is to compare a small and a large milling engagement with the same maximal cut thickness h_{max} equal to 96 µm. This helps to see the influence of the teeth contact cutting time on tool wear. These two configurations are tested four times on each material which means that 16 tools are used during these tests. The depth of cut is equal to 2 mm for all tests. As a consequence, tool life is examined towards machined volume.

Table 6. Milling conditions for small and large engagement configurations (h_{max} = 96 µm).

Configuration	V_c (m/min)	f_z (mm/rev/tooth)	a_e (mm)	a_p (mm)
Small	40	0.16	1	2
Large	40	0.098	4	2

The observations in Fig. 12 show the wear process in milling WRT material, but the principal manifestations of tool wear seem to be the same for both material and both configuration. One macro wear mechanism consists in a notching at the depth of cut limit, where material is going to smear in it. On the other part of the cutting edge a pure flank wear is observed. Then, the smeared material is going to be snatched from the flank face increasing by this way the notching dimension as presented in Fig. 13.
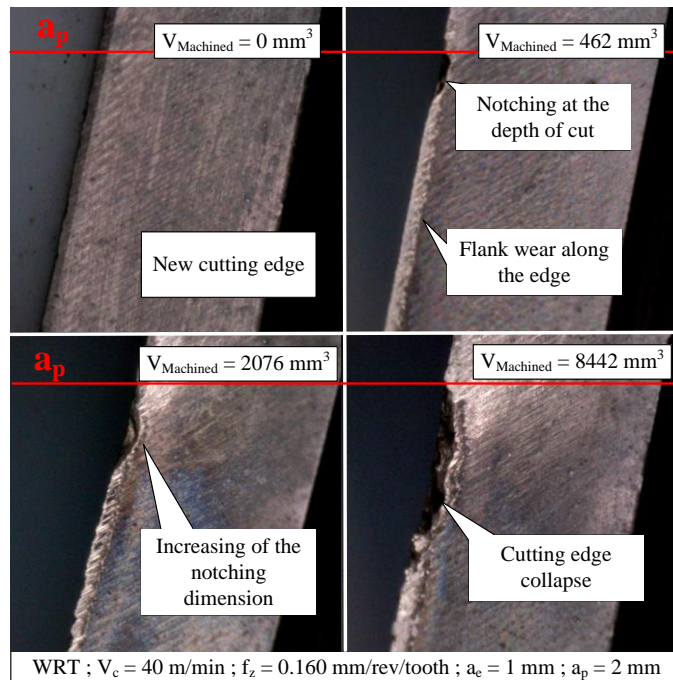

WRT ; V_c = 40 m/min ; f_z = 0.160 mm/rev/tooth ; a_e = 1 mm ; a_p = 2 mm

Fig. 12. Tool wear characterisation in end milling of WRT Inconel 718.

Another wear manifestation is based on the previous one but the initial state is a scratch on the cutting edge due to a carbide from the machined material. However, the initial notching is not localised. So this mechanism produces random wear profile. Sometimes the material smeared on the flank face may stay for a long period creating a build-up edge and protect the cutting edge. Consequently, this protection increases tool life. All mechanisms lead to cutting edge collapse.
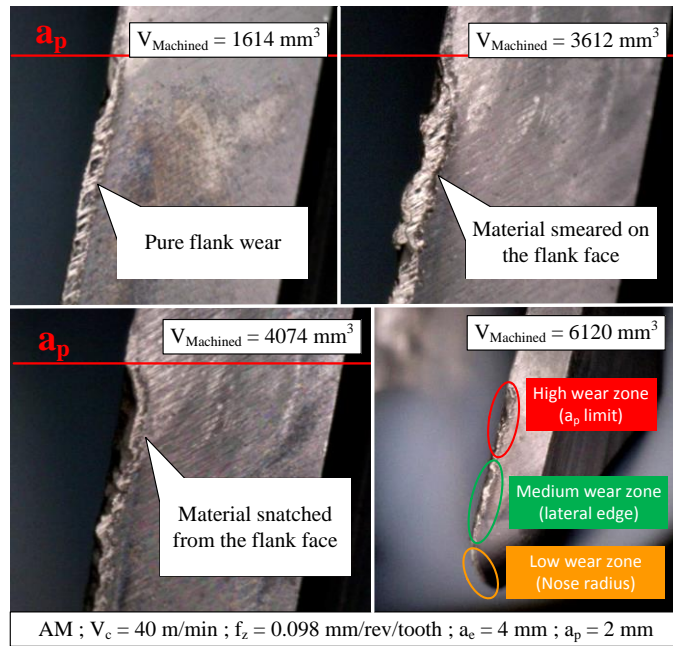
Fig. 13. Tool wear observation from flank wear to cutting edge collapse in end milling of AM Inconel 718.

The Fig. 14 illustrates the evolution of maximal flank wear towards all tool cutting edges $VB_{max/max}$. It transposes the range of flank wear measured during 4 wear test for each condition. The tool life in WRT material is approximatively half the one in AM material, with considering $VB_{max/max} = 0.3$ mm as a limit. This is due to higher cutting forces for the same cut thickness as seen in the fresh tool model which conduct quickly to a critical tool wear. Moreover as carbides are larger in WRT material, they are more likely to produce scratch on the flank face and lead to an increase of the tool wear following the second manifestation presented earlier as presented by Dudzinski et al. [13].

Concerning tool engagement, the higher is the engagement, the lower is the tool life in term of machined volume. This observation is due to the time contact between the material and the cutting edge. At the same cutting speed, the radial engagement sets the cutting contact time. Therefore, the higher this time is, the higher the edge temperature would be. As the temperature is a leading factor in tool wear, tool life is longer with a small engagement.
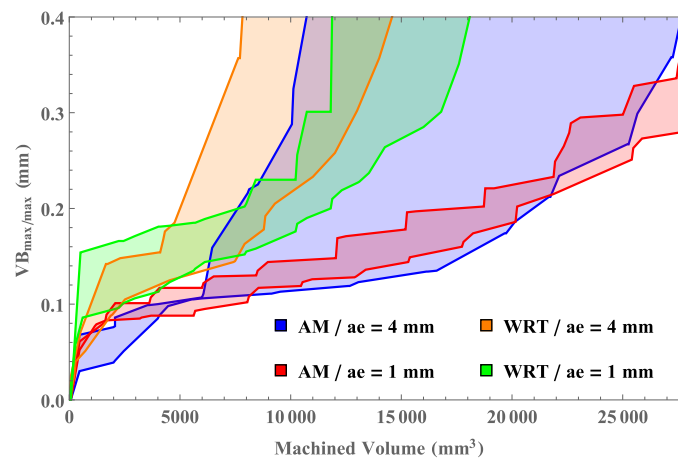

Fig. 14. Flank wear evolution range (4 wear tests) as a function of machined volume respectively for AM and WRT material and for both engagements.

Consequently, these investigations demonstrate that AM material has a better machinability, regarding cutting forces and global tool wear, than WRT one.

4.2. Wear impact on cutting forces and tool model update

The evolution of cutting forces towards tool wear must be characterised in order to later model them precisely over a long time. In a first approach cutting forces are recorded at different wear states. Results are presented in Fig. 15 with teeth cutting discontinuity conditions. It is observed that evolution of tool wear has a modest impact on $\{\overline{F_X}\}_{Meas/WPF}$. The different levels of initial cutting force peaks are a consequence of the initial runout of each teeth; the peak is higher for teeth having a high runout. Thus, a cutting edge with such high initial runout is going to generate higher cutting forces and to wear out faster. Finally, due to wear, the measured cutting forces peak increases for teeth with the smallest initial $\{\overline{F_X}\}_{Meas/WPF}$ whereas it decreases for teeth with the highest initial $\{\overline{F_X}\}_{Meas/WPF}$. This observation shows that tool wear is first a tool geometry modification as it tends to reduce runout. That is why needs to be implemented in the tool modelling.

Concerning $\{\overline{F_Y}\}_{Meas/WPF}$ in Fig. 15, the cutting forces gradually increase with tool wear. This observation shows that tool wear is also an alteration of the surfaces interaction between the tool and the work material. This interaction can be modelled by a modification of the local cutting model in TRA. Finally, a major increase on both $\{\overline{F_X}\}_{Meas/WPF}$ and $\{\overline{F_Y}\}_{Meas/WPF}$ is located when the cutting edges exit work material whereas cutting forces are very similar at the cutting edge entrance. This is due to the non-constant wear profile along the cutting edge as show in Fig. 13. That is why the VB profile along the cutting edge has to be considered.
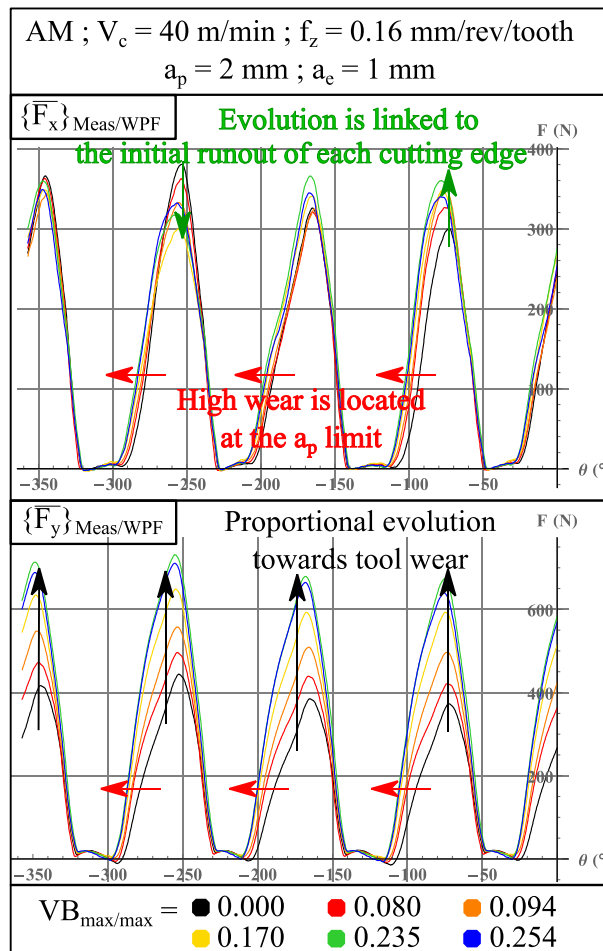

Fig. 15. Cutting forces measurement and their evolutions in X (a) and Y (b) directions towards tool wear.

The geometrical tool evolution due to wear and its change of runout is integrated into the tool model as following. Considering a pure flank wear, the Back off Cutting Edge (BCE) is a function of the flank wear VB and the clearance angle α_o by Eq (11):

$$BCE[i_{Fl},z] = VB[i_{Fl},z].\tan(\alpha_o) \tag{11}$$

Next step, the VB profile is computed based on the VB_{max} measure on each cutting edge and takes into account the different wear zone presented in Fig. 13. An exponential function has been used to model VB along the cutting edge as shown in Fig. 16 and Eq (13).
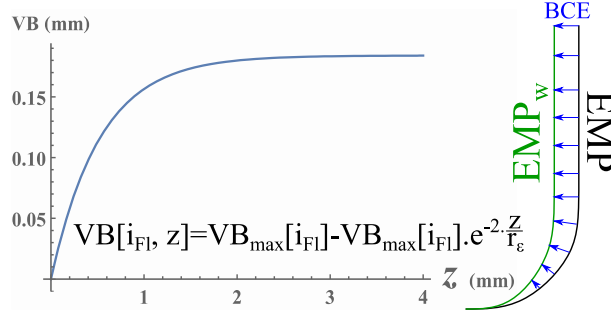

Fig. 16. Modelling wear profile with VB_{max} measurement.

$$VB[i_{Fl},z] = VB_{max}[i_{Fl}].\left(1 - e^{-2\frac{z}{r_\varepsilon}}\right) \tag{12}$$

Finally, the actual cutting edge is established thanks to Eq (1) based on the worn end mill profile $\underline{EMP_w}$. This profile is depicted in Eq (13) considering a BCE of EMP into $-\underline{NV_{EMP}}$ way; the normal vector to the initial tool profile $\underline{EMP}$.

$$\underline{EMP_w}[i_{Fl},z] = \underline{EMP}[z] - BCE[i_{Fl},z].\underline{NV_{EMP}}[z] \tag{13}$$

For z higher than the tool nose radius r_ε, the tool geometry modification generates a runout modification. Thus, it is possible to compare the model evolution with the measured runout evolution. In order to validate the propose approach, the runout is now measured with an electronic dial indicator of 1 μm resolution. The results are shown in Fig. 17. The measured runout evolution matches with its evaluation from VB measurement according to Eqs. (11) and (13). It confirms the tool model evolution towards its wear developed in this section. The VB profile considers a pure flank wear and a not random effect. Thus, only the first mechanism presented in the section 4.1 is modelled. Moreover, as the wear increasing, the edge collapse can produce a high variation in the wear profile and affect the cutting geometry and then the forces. That is why only flank wear inferior at 0.25 mm can be examined.
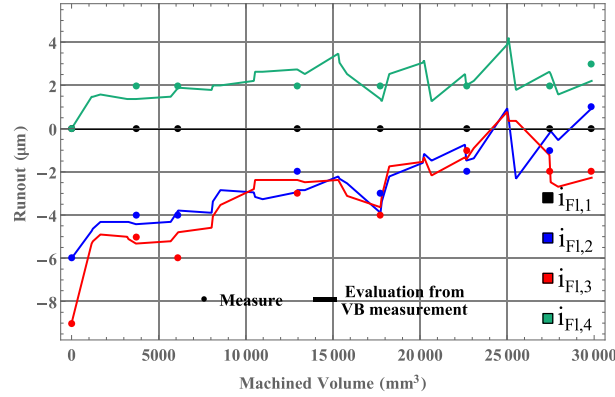

Fig. 17. Tool radial runout computed considering VB measurement and actual measured runout for AM material and $a_e = 1$ mm.

4.3. Cutting force model including tool wear effect

As described in section 4.2, tool wear effect must be included into the local mechanistic model to integrate the modification of the interaction between the tool and the machined material. It is proposed in Eq. (14) a mechanistic model for local cutting forces in TRA considering tool wear.

$$\{f_t[i_{Fl},\theta]\}_{TRA_{iz}} = b_{iz}\left(K_{tb}\underbrace{(1+K_{tw}.VB_{iz}[i_{Fl}])}_{Tool\ wear\ effect} + K_{th}.h_{iz}[i_{Fl},\theta]\right)\left(1+K_{t\lambda}.\lambda_{s_{iz}}\right)$$

$$\{f_r[i_{Fl},\theta]\}_{TRA_{iz}} = b_{iz}\left(K_{rb}\underbrace{(1+K_{rw}.VB_{iz}[i_{Fl}])}_{Tool\ wear\ effect} + K_{rh}.h_{iz}[i_{Fl},\theta]\right)\left(1+K_{r\lambda}.\lambda_{s_{iz}}\right) \qquad (14)$$

$$\{f_a[i_{Fl},\theta]\}_{TRA_{iz}} = b_{iz}\left(K_{ab}\underbrace{(1+K_{aw}.VB_{iz}[i_{Fl}])}_{Tool\ wear\ effect} + K_{ah}.h_{iz}[i_{Fl},\theta]\right).\lambda_{s_{iz}}$$

This model is identified with the process shown in section 3.3. Nevertheless, the coefficients representing the edge, the cut and the obliquity effect are limited around the ones identified previously for a fresh tool. Identified coefficients for Eq. (14) are presented in Table 4 and the trials used for the identification are shown in Table 7. As for fresh tool, the coefficients variations are due to identification deviation or local tool geometry variation. The cut, edge and obliquity effects coefficients are the same as for fresh tool because for VB equal to 0 the model for used tool is equal to the model for fresh tool. The wear coefficient K_{aw} for axial direction in TRA is negligible as the edge one K_{ab} for both material. It means that the chip flow direction does not change towards wear evolution. Nevertheless, they are not set to 0 to limit identification instability.

The same analysis illustrated in section 3.4 concerning the macroscopic friction coefficient is done with the wear coefficient added to the computation. The wear has no impact on the coefficient Cf_{Rake} for both material as wear coefficient is applied to the edge effect. The coefficient $Cf_{Flank,w}$ is equal to 1.22 for WRT and 0.61 for AM. It confirms the conclusion seen in section 3.4.

The Fig. 18 presents the evolution of cutting forces over tool wear, modelled vs experiments, for one milling test in AM Inconel 718. For these conditions, there is no teeth cutting continuity and flank wear levels of each tooth are given. This results show that tool wear has not only a repercussion on the cutting forces peak but also on the curves forms. It also shows that greater is the tool wear, lower is the prediction precision. The causes of this effect are the model hypotheses, indeed in high wear state the tool has not been only damaged on the flank face and not only according to the profile presented in section 4.2. Furthermore, the fresh tool is coated and this coating (2 μm) may be not present anymore at high wear state which highly changes the friction coefficient between the tool and the chip creating hazard effect such as build up edge.
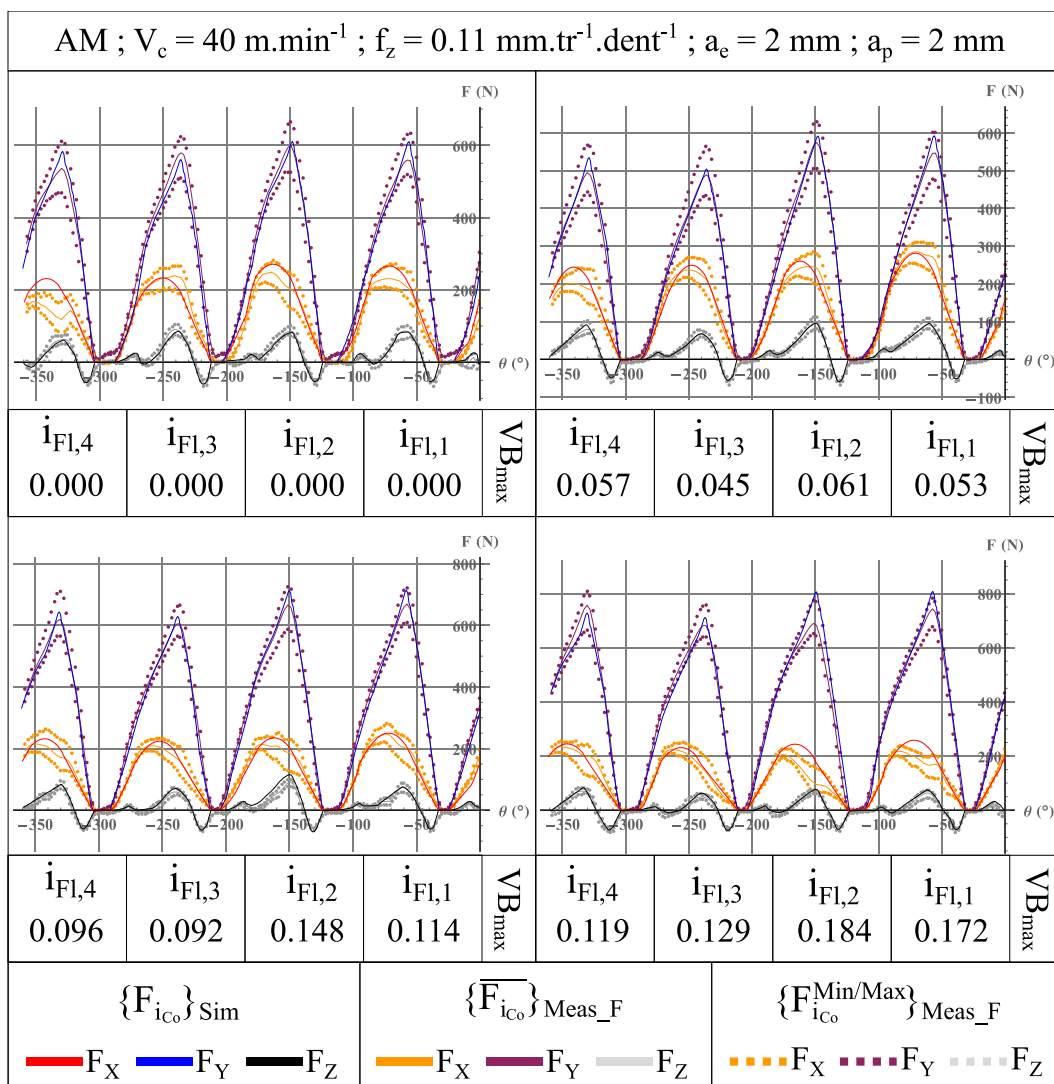
Fig. 18. Cutting forces simulated and measured during milling of AM Inconel 718 with worn tool.

The Table 7 presents the absolute error and the absolute difference between minimal and maximal measured cutting forces. It shows that only $Error_Y$ in the <u>Y</u> direction is higher than experimental force variation over revolution ΔF_Y, but for AM material the difference is only of 2 N. Moreover, the InValue for both materials is around 75 %, but on Fig. 18 the out pipe simulation are concentrated on trials with high tool

wear. As shown in section 4.2, the profile is modelled according tool wear in a pure flank wear hypothesis. This hypothesis limits the model validity to low wear state as high wear would create random profile.

Table 7. Identification and validation trials for mechanistic model with worn tool.

N° Trial	Usage	V_c (m/min)	f_z (mm/rev/tooth)	a_e (mm)	a_p (mm)	$VB_{max/max}$ (mm)
1	Id/Val	40	0.098	4	2	0.000
2	Id/Val	40	0.098	4	2	0.065
3	Id/Val	40	0.098	4	2	0.153
4	Id/Val	40	0.110	2	2	0.000
5	Id/Val	40	0.110	2	2	0.061
6	Id/Val	40	0.110	2	2	0.148
7	Id/Val	40	0.110	2	2	0.184
8	Id/Val	40	0.160	1	2	0.000
9	Id/Val	40	0.160	1	2	0.052
10	Id/Val	40	0.160	1	2	0.099
11	Id/Val	40	0.160	1	2	0.149
12	Val	40	0.098	4	2	0.095
13	Val	40	0.098	4	2	0.225
14	Val	40	0.110	2	2	0.089
15	Val	40	0.110	2	2	0.218
16	Val	40	0.160	1	2	0.205

	ΔF_X (N)	$Error_X$ (N)	ΔF_Y (N)	$Error_Y$ (N)	ΔF_Z (N)	$Error_Z$ (N)	$Error_{XYZ}$ (%)	InValue (%)
WRT	49	43	67	70	14	16	9.9	75
AM	51	45	61	63	11	12	8.9	77

5. Conclusion

The purpose of this work is to analyse the machinability of additive manufactured Inconel 718 in side milling with rounded solid carbide cutters. To this end, the work material microstructure, wear mechanisms, the cutting forces affected by tool wear are studied for both the additive manufactured Inconel 718 and a wrought Inconel 718. Then, it is developed a mechanistic approach to model cutting forces based on a fully geometrically defined parametrisation including real runout along cutting edge with a precise cut thickness determination, with using the cutting edge discretisation methodology. It includes at first step a fresh tool and then considering tool wear. The main conclusions are:

- In machining additive manufactured Inconel 718, cutting forces are lower in all direction compare to machining wrought Inconel 718 which could be explained by the difference of microstructure
- The main tool wear mechanism is abrasion on the flank face which leads to edge collapsing through attrition of the cutting edge by material stocked and snatched from the flank face.
- A second tool wear process is notching at the depth of cut and where carbides damage the cutting edge.
- A final process is the cutting edge protection by smeared material on the flank face and built-up edge formation.
- Tool life in wrought Inconel 718 is half the tool life in additive manufactured one.
- The tool wear has an impact on the tool geometry and its model has to follow this geometrical evolution (runout).
- The tool wear also affects significantly and directly cutting forces and so has to be considered into local model formulation as proposed.
- It is difficult to consider critical tool wear effect (VB_{max} greater than 0.25 mm) in a predictive model as it creates too many random wear profile.

In addition, this article deeply formulated several methods to have a robust model identification and to characterize its precision, these aspects are often eclipsed from comparable study. The first method consists in considering the cutting forces variation, over tool revolutions, in the measurement treatment to create the measured pipe. The second one is to validate the model identification and simulation data through several criteria. The last one is to examine identified coefficients and their relation to physical properties observed.

6. References

1. Wang Xiaoqing. Gong X and Chou K. Review on powder-bed laser additive manufacturing of Inconel 718 parts. *Proceedings of the Institution of Mechanical Engineers, Part B: Journal of Engineering Manufacture*. (2017). Vol. 231, p. 1890–1903.

2. Chlebus E. Gruber K. Kuznicka B. Kurzac J and Kurzynowski T. Effect of heat treatment on the microstructure and mechanical properties of Inconel 718 processed by selective laser melting. *Materials Science and Engineering: A*. (2015). Vol. 639, p. 647–655.

3. Altintas Yusuf. Manufacturing Automation: Metal Cutting Mechanics, Machine Tool Vibrations, and CNC Design. *Cambridge University Press*. (2012).

4. Armarego E.J.A and Epp C.J. An investigation of zero helix peripheral up-milling. *International Journal of Machine Tool Design and Research*. (1970). Vol. 10, no. 2, p. 273–291.

5. Armarego E.J.A and Deshpande N.P. Computerized Predictive Cutting Models for Forces in End-Milling Including Eccentricity Effects. *CIRP Annals*. (1989). Vol. 38, no. 1, p. 45–49.

6.   Kaymakci M. Kilic Z.M. and Altintas Y. Unified cutting force model for turning, boring, drilling and milling operations. *International Journal of Machine Tools and Manufacture*. (2012). Vol. 54–55, p. 34–45.

7.   Fromentin Guillaume and Poulachon Gérard. Geometrical analysis of thread milling — part 2: calculation of uncut chip thickness. *The International Journal of Advanced Manufacturing Technology*. (2010). Vol. 49, no. 1, p. 81–87.

8.   Killic Z. M. and Altintas Yusuf. Generalized modelling of cutting tool geometries for unified process simulation. *International Journal of Machine Tools and Manufacture*. (2016). Vol. 104, p. 14–25.

9.   Zheng H.Q. Li X.P. Wong Y.S. and Nee A.Y.C. Theoretical modelling and simulation of cutting forces in face milling with cutter runout. *International Journal of Machine Tools and Manufacture*. (1999). Vol. 39, no. 12, p. 2003–2018.

10.   Ozturk Erdem. Ozkirimli O. Gibbons T. Saibi M and Turner S. Prediction of effect of helix angle on cutting force coefficients for design of new tools. *CIRP Annals*. (2016). Vol. 65, no. 1, p. 125–128.

11.   Niu Jimbo. Ding Ye. Zhu LiMin and Ding Han. Mechanics and multi-regenerative stability of variable pitch and variable helix milling tools considering runout. *International Journal of Machine Tools and Manufacture*. (2017). Vol. 123, p. 129–145.

12.   Bissey-Breton S. Poulachon G. and Lapujoulade F. Integration of tool geometry in prediction of cutting forces during milling of hard materials. *Proceedings of the Institution of Mechanical Engineers, Part B: Journal of Engineering Manufacture*. (2006). Vol. 220, no. 4, p. 579–587.

13.   Dudzinski D. Devillez A. Moufki A. Larrouquère D. Zerrouki V and Vigneau J. A review of developments towards dry and high speed machining of Inconel 718 alloy. *International Journal of Machine Tools and Manufacture*. (2004). Vol. 44, no. 4, p. 439–456.

14.   Oraby S.E and Hayhurst D.R. Development of models for tool wear force relationships in metal cutting. *International Journal of Mechanical Sciences*. (1991). Vol. 33, no. 2, p. 125–138.

15.   Li Kuan-Ming and Liang Steven Y. Modeling of cutting forces in near dry machining under tool wear effect. *International Journal of Machine Tools and Manufacture*. (2007). Vol. 47, no. 7–8, p. 1292–1301.

16.   Sun Yujing. Sun Jie. Li Jianfeng. Li Weidong and Feng Bin. Modeling of cutting force under the tool flank wear effect in end milling Ti6Al4V with solid carbide tool. *International Journal of Advanced Manufacturing Technology*. (2013). Vol. 69, no. 9, p. 2545–2553.

17.   Pan Zhipeng. Feng Yixuan and Liang Steven. Material microstructure affected machining: a review | Manufacturing Review. *Manufacturing review*. (2017). Vol. 4, no. 5, p. 12–23.

18.   Kamdar Madhusudan Henry. Embrittlement by liquid metals. *Progress in Materials Science*. (1973). Vol. 15, no. 4, p. 289–374.

19.   ASTM E112-13. Standard Test Methods for Determining Average Grain Size. *ASTM International, West Conshohocken, PA*. (2013).

20.   Karasev Andrey. Alekseeva Ekaterina. Lukianov Aleksey and Jönsson Pär G. Characterization of non-metallic inclusions in corrosion -resistance nickel - based EP718 and 718 alloys by using electrolytic extraction method. *E3S Web of Conferences*. (2019). Vol. 121, p. 04004.

21.   ISO 3002-1:1982. Basic quantities in cutting and grinding -- Part 1: Geometry of the active part of cutting tools -- General terms, reference systems, tool and working angles, chip breakers. *ISO* [online]. [Accessed 17 December 2018].

23.   ISO 8688-2:1989. Tool life testing in milling - Part 2: End milling. [online]. [Accessed 28 February 2020].

24.   Devillez A. Schneider F. Dominiak S. Dudzinski D. and Larrouquere D. Cutting forces and wear in dry machining of Inconel 718 with coated carbide tools. *Wear*. (2007). Vol. 262, no. 7, p. 931–942.